iScience

Article

Dual-functional silver nanoparticle-enhanced ZnO nanorods for improved reactive oxygen species generation and cancer treatment

Graphical abstract

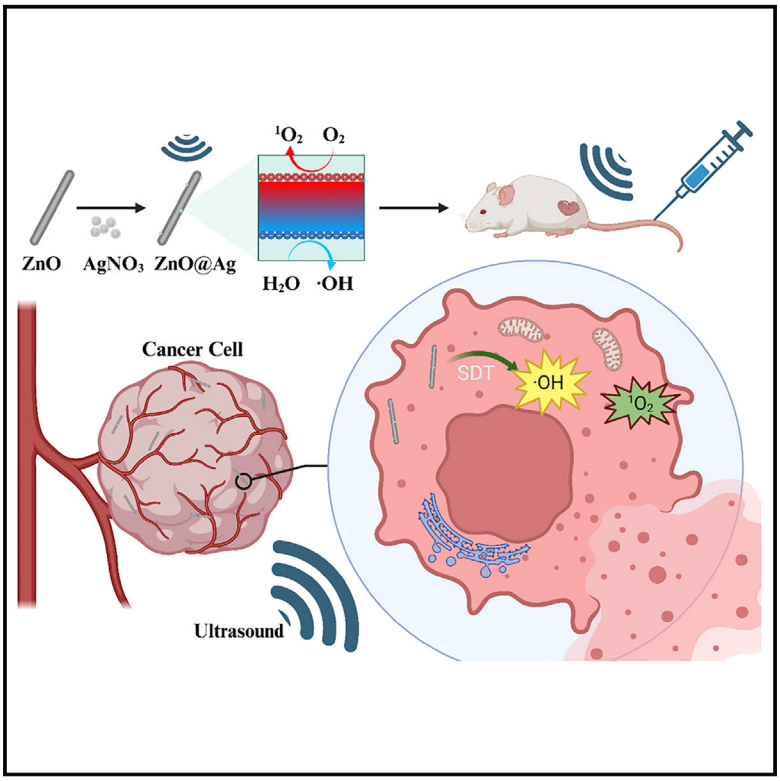

Highlights

- ZnO@Ag NRs enhance ROS generation under ultrasound through efficient electron-hole separation
- Combined ZnO@Ag NRs and ultrasound treatment significantly inhibit tumor growth *in vivo*
- ZnO@Ag NRs exhibit excellent biocompatibility and intrinsic antibacterial properties

Authors

Yichao Tao, Wenbin Zhuang, Wensi Fan, Longxiang Zhou, Lihong Fan, Huanlong Qin, Yefei Zhu

Correspondence

1300008@tongji.edu.cn (L.F.), huanlongqin@yeah.net (H.Q.), yefei_zhu@foxmail.com (Y.Z.)

In brief

Therapeutics; Cancer; Materials science; Nanomaterials

Tao et al., 2025, iScience *28*, 111858
February 21, 2025
https://doi.org/10.1016/j.isci.2025.111858

CellPress

iScience

CellPress
OPEN ACCESS

Article

Dual-functional silver nanoparticle-enhanced ZnO nanorods for improved reactive oxygen species generation and cancer treatment

Yichao Tao,[1,2,3,6] Wenbin Zhuang,[1,2,6] Wensi Fan,[2,6] Longxiang Zhou,[4] Lihong Fan,[1,2,*] Huanlong Qin,[1,2,*] and Yefei Zhu[5,7,*]

[1]School of Medicine, Nantong University, Nantong 226001, China
[2]Shanghai Tenth People's Hospital, School of Medicine, Tongji University, Shanghai 200072, China
[3]Zhangjiagang Hospital of Traditional Chinese Medicine, Suzhou 215600, China
[4]Department of General Surgery, Jinshan Central Hospital Affiliated to Shanghai University of Medicine & Health Sciences, No.147, Jiankang Road, Shanghai 201599, China
[5]Department of Gastroenterology, Affiliated Hospital of Yangzhou University, Yangzhou University, Yangzhou 225001, China
[6]These authors contributed equally
[7]Lead contact
*Correspondence: 1300008@tongji.edu.cn (L.F.), huanlongqin@yeah.net (H.Q.), yefei_zhu@foxmail.com (Y.Z.)
https://doi.org/10.1016/j.isci.2025.111858

SUMMARY

Recent advancements in sonodynamic therapy (SDT) for cancer treatment have highlighted the potential of enhancing reactive oxygen species (ROS) generation and improving therapeutic outcomes. This study introduces zinc oxide (ZnO) nanorods (NRs) *in situ* loaded with silver nanoparticles (ZnO@Ag NRs), designed to optimize ROS production under ultrasound irradiation and offer significant advantages in tumor specificity and biosafety. The transmission electron microscopy and elemental mapping confirmed the consistent size and monodispersed Ag nanoparticle for ZnO@Ag NR. Sonodynamic properties showed that ZnO@Ag NRs produce higher singlet oxygen and hydroxyl radicals under ultrasound. *In vitro* studies demonstrated excellent biocompatibility and enhanced cell-killing effects of ZnO@Ag NRs on CT-26 cells, while *in vivo* results confirmed its superior anti-tumor efficacy and biosafety. Furthermore, the ZnO@Ag NRs' antibacterial properties were also confirmed, suggesting additional benefits in treating cancers associated with bacterial infections. Collectively, these findings establish ZnO@Ag NRs as a potent and safe agent for ultrasound-driven cancer therapy.

INTRODUCTION

Recent years have seen increasing interest in cancer treatments that regulate reactive oxygen species (ROS), including singlet oxygen ($^1O_2$), superoxide radical ($O_2\cdot^-$), and hydroxyl radical ($\cdot OH$).[1] Oxidative stress induced by ROS leads to effective, cancer-specific cell death.[2] Recent advances in catalytic chemistry, particularly catalytic Fenton reactions, provide practical methods for generating ROS through redox reactions.[3–5] Dynamic therapies using nanomaterials that generate excessive toxic ROS have significant cancer treatment advantages due to their non-invasiveness and high selectivity.[6] By enhancing permeability and retention (EPR), nanoparticles facilitate not only their internalization by cancer cells but also their selective accumulation in tumors.[7] Although the large surface area of nanoparticles enhances ROS production, excessive ROS can irreversibly damage cellular components like organelles and the cytoskeleton, leading to tumor cell destruction.[8] Non-invasive treatments like photodynamic therapy (PDT) and sonodynamic therapy (SDT), known for their precise control and minimal side effects, have been extensively studied.[9–11] Specifically, SDT excels over PDT in terms of deeper tissue penetration, uniform energy absorption, and enhanced biosafety.[12,13] Recent reviews have comprehensively discussed the advances in inorganic sonosensitizers and their ROS-generating capabilities, providing a foundation for the development of novel SDT agents.[14,15] Currently, SDT utilizes two primary types of sonosensitizers: organic substances and inorganic nanomaterials.[16–18] In addition to having poor hydrophobicity, low bioavailability, rapid elimination, and insufficient tumor accumulation, organic sonosensitizers are often difficult to use.[16,19] In contrast, inorganic sonosensitizers are promising for SDT applications due to their ultrasound stability, tumor specificity, and prolonged circulation. However, the development of additional inorganic sonosensitizers is critical to address the growing therapeutic demands in both research and clinical applications.[20]

Ultrasound (US) exhibits characteristics similar to light spectrums across various wavelengths in SDT, which may activate specific semiconductors based on the fundamental mechanisms of sonoluminescence.[21,22] The activators in a semiconductor

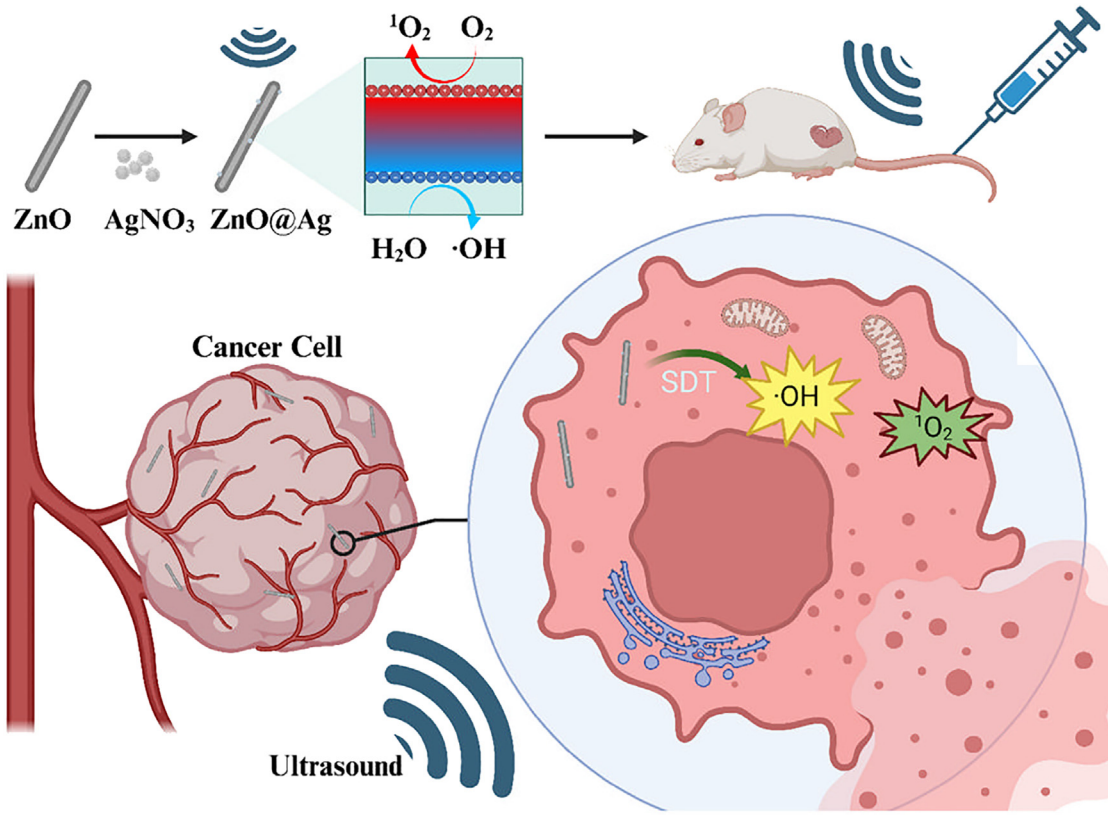

Figure 1. Schematic diagram of treatment with enhanced sonodynamics after intravenous injection of ZnO@Ag NRs into a colorectal tumor-bearing mouse

cause electron to be excited from the valence band to the conduction band as ultrasound energy is absorbed by it.[23–25] These electrons move to the material's surface, catalyzing redox reactions that transform adsorbed O_2 into toxic $^1O_2$.[26] Given the pivotal role of electrons, semiconductors with suitable bandgap structures are essential for effective electron-hole separation. Constructing heterostructures is crucial for improving quantum yield. Coupling semiconductor materials or noble metals with a base semiconductor forms heterostructures that enhance spatial charge separation via electron transfers between components.[27–29] This configuration allows for the effective spatial separation of electrons and holes induced by acoustic waves.[30–32] Therefore, the selection of semiconductors with suitable bandgaps and Fermi level interactions is essential for developing advanced sonosensitizers that guarantee efficient electron-hole separation.[33,34] This insight underscores the crucial importance of carefully designed heterostructures in boosting both the efficiency and efficacy of sonodynamic cancer therapy.[35]

Zinc oxide nanorods (ZnO NRs), extensively studied for their unique piezoelectric properties, owe these features to their non-centrosymmetric crystal structure. ZnO NRs exhibit a piezoelectric effect when exposed to ultrasound irradiation, indicating their potential as piezocatalysts. Although promising, piezocatalytic treatment currently faces limitations, notably its relatively low capability for ROS generation.[36] In this study, we specifically designed ZnO nanorods (NRs) that *in situ* loaded Ag nanoparticle (NPs), termed ZnO@Ag NRs. Featuring a strategic bandgap,[37] ZnO@Ag NPs offer an alternative as an SDT agent. The heterostructure of ZnO@Ag NRs is constructed through the conordination-redox reaction of Ag on the surface of ZnO NRs. ZnO@Ag nanorods (NRs) form a heterojunction due to the difference in Fermi levels between ZnO and Ag. This heterojunction facilitates efficient electron-hole separation, which is critical for enhancing reactive oxygen species generation under ultrasound irradiation. As shown in Figure 1, ZnO@Ag NRs effectively separate electrons and holes under ultrasound, thereby enhancing SDT mechanics and increasing ROS generation, which accelerates tumor death. Additionally, ZnO nanorods alone are known to exhibit antibacterial properties, as demonstrated in previous studies.[38] The incorporation of silver nanoparticles further enhances these properties, providing a synergistic effect that improves the overall antibacterial efficacy of ZnO@Ag NRs. Consequently, this study lays the groundwork for a promising ultrasound-driven tumor treatment platform, potentially inspiring further development of more effective treatment strategies.

RESULTS

Synthesis and characterization of ZnO@Ag

ZnO nanorods were synthesized and loaded with Ag nanoparticles using a well-established $NaBH_4$ reduction method[39] (Figure 2A). Transmission electron microscopy (TEM) results

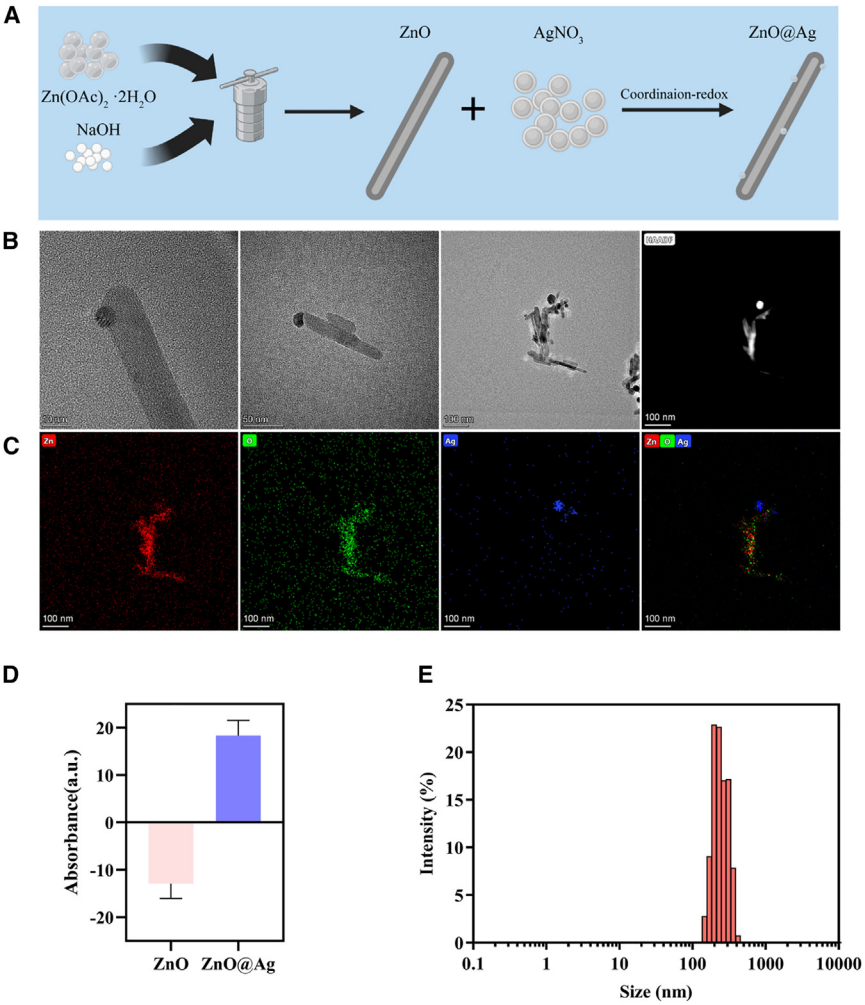

Figure 2. Characterization of ZnO@Ag

(A) Schematic representation for ZnO@Ag NRs synthesis.

(B) Representative TEM image for ZnO@Ag NRs. Scale bar, 10 nm, 50 nm, 100 nm, individually.

(C) Elemental mapping image of the distribution of Ag, Zn, and O in ZnO@Ag NRs. Scale bar, 100 nm.

(D) The zeta potential results for ZnO@Ag NRs and ZnO NRs.

(E) The dynamic light scattering result for ZnO@Ag NRs sample. Data are represented as mean ± SD.

revealed ZnO@Ag NRs were approximately 220 nm in length, with uniformly distributed Ag nanoparticles on the surface, exhibiting ideal monodispersity (Figure 2B). Dark-field imaging further confirmed the successful deposition of Ag nanoparticles. Elemental mapping depicted the distribution of Ag, Zn, and O in the ZnO@Ag, confirming the successful synthesis of the heterostructure (Figure 2C). The synthesis of ZnO@Ag results in the formation of a heterostructure, where Ag nanoparticles are in close contact with ZnO nanorods. This heterojunction allows for efficient charge transfer, with Ag acting as an electron sink that prevents the recombination of photoexcited electron-hole pairs. This structural feature is expected to enhance the catalytic properties of ZnO@Ag. The zeta potentials were measured as −16.04 mV for ZnO and 15.21 mV for ZnO@Ag, respectively (Figure 2D). The average size of ZnO@Ag NRs was about 240 nm, consistent with previous electron microscopy findings (Figure 2E).

The sonodynamic properties of ZnO and ZnO@Ag NRs

We employed electron spin resonance (ESR) spectroscopy with 2,2,6,6-tetramethylpiperidine (TEMP) as the probe for detecting $^1O_2$, as shown in Figure 3A. TEMP reacts specifically with $^1O_2$ to form TEMP-$^1O_2$, which generates a characteristic 1:1:1 triplet ESR signal under ultrasound conditions (1.5 W/cm^2, 50% duty cycle, 1 MHz). This method is widely recognized for detecting singlet oxygen in SDT systems.[12,31] Although the 9,10-Anthracenediyl-bis (methylene)dimalonic acid (ABDA) assay is commonly used in photodynamic therapy (PDT), the TEMP-based ESR method provides direct and reliable confirmation of $^1O_2$ in our study. As demonstrated by the ESR data, the ZnO@Ag NRs exhibit significantly enhanced $^1O_2$ generation under ultrasound irradiation compared to ZnO NRs alone. The 1:1:1 triplet signal from the TEMP spin trap in Figure 3A indicated $^1O_2$ generation in the ZnO + US group, with a more intense signal observed in the ZnO@Ag + US group. Typically, no significant signal was observed for ZnO or ZnO@Ag without US, indicating that US is essential for their $^1O_2$ generating ability, and that ZnO@Ag has a significantly better catalytic effect than ZnO. 5,5-Dimethyl-1-pyrroline N-oxide (DMPO) was used as an ·OH indicator to access the ·OH generation ability of both NRs under the same US conditions and without, using the ESR method. A 1:2:2:1 signal from the DMPO spin trap in Figure 3B indicated ·OH generation in the ZnO + US group, with a more intense signal in the ZnO@Ag + US group. Similarly, no significant signal was detected for ZnO or ZnO@Ag without US, underscoring the necessity of US for ·OH generation. Once again, this conformed the superior catalytic effect of ZnO@Ag. Furthermore, 3,3′,5,5′-tetramethylbenzidine (TMB) was used as an indicator to measure hydroxyl radical generation under US conditions (1.5 W/cm^2, 50% duty cycle, 1 MHz). A distinct 370 nm absorption peak indicated the formation of blue ox-TMB from the reaction between TMB and hydroxyl radicals under oxidative conditions. The ultraviolet (UV) spectral results revealed that after a 4-min US treatment, the characteristic absorption peak of the ZnO@Ag + US group was higher than that of in ZnO + US group, highlighting ZnO@Ag's superior hydroxyl radical generating ability, attributed primarily to its unique

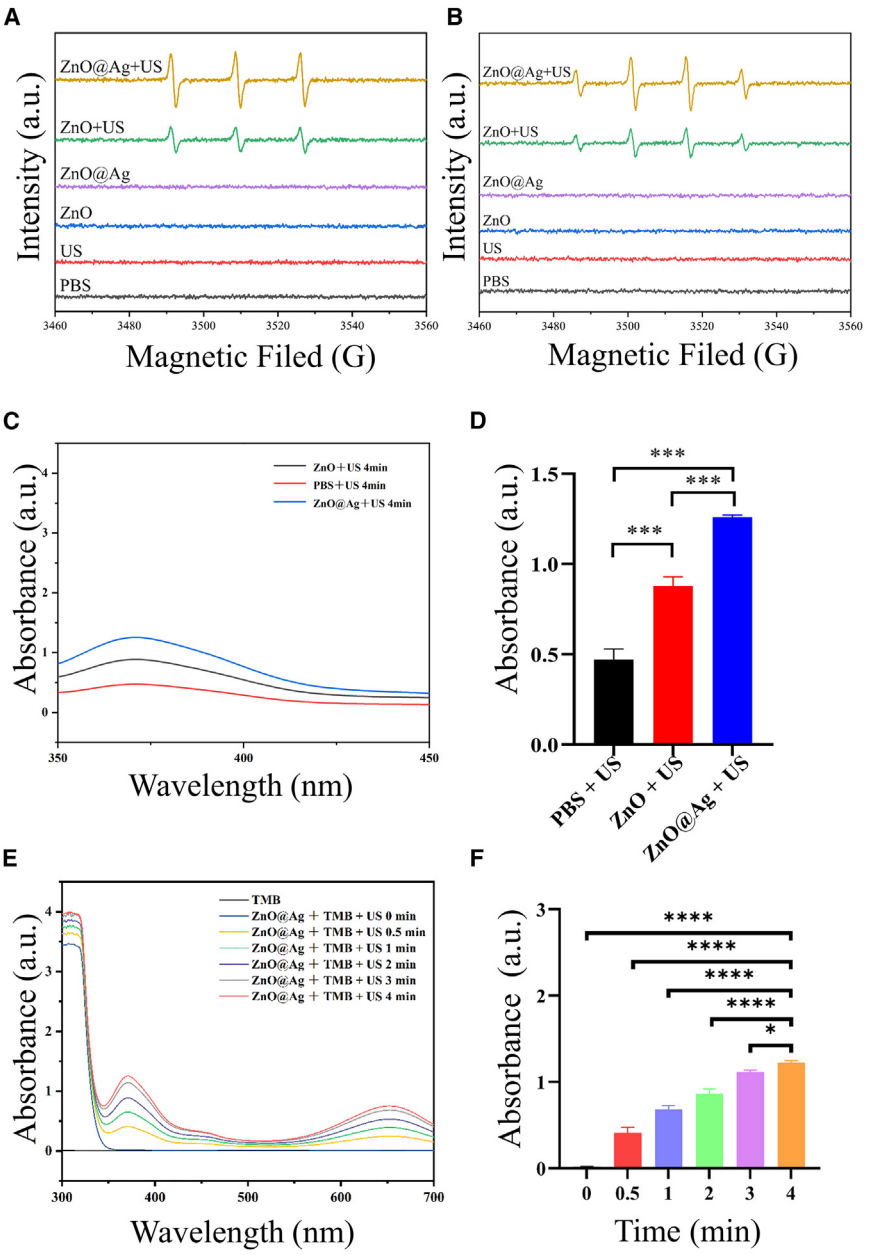

Figure 3. The sonodynamic properties of ZnO and ZnO@Ag NRs

(A) The ESR results of $^1O_2$ generation in all groups.

(B) The ESR results of ·OH generation in all groups.

(C) The UV spectral results of ·OH generation in all groups.

(D) The statistical analyses results of the absorbance at 370 nm in all groups.

(E) The UV spectral results of ZnO@Ag NRs after different US treating times.

(F) The statistical analyses result of the absorbance at 370 nm ZnO@Ag NRs undergoing different US treating times.

Data are represented as mean ± SD, "*" means $p < 0.05$, "****" means $p < 0.001$, "*****" means $p < 0.0001$.

electronic band structure and significant sonodynamic effects (Figure 3C). We conducted statistical analyses and tests on the 370 nm value, which confirmed similar findings (Figure 3D). Additionally, using similar methods, we investigated the ROS production properties of ZnO@Ag; the characteristic absorption peak increased over time, with the strongest peak observed in the 4-min US treatment group, indicating that the ·OH generation ability of ZnO@Ag depended on the duration of US treatment (Figure 3E). The statistical analysis of the 370 nm value (Figure 3F) and 650 nm value (Figure S1) yielded similar results. Our results confirmed that ZnO NRs exhibit an absorption band around 373 nm, consistent with previous research[40] (Figure S2). However, the absorbance value of ZnO NRs at 373 nm is not large enough to interfere with or mask the ox-TMB results on the 370 nm value due to its low concentration of use. In conclusion, our findings confirmed that the ROS production ability of ZnO@Ag exceeded that of ZnO and is highly depended on the duration of US treatment in this study.

To validate the electron/hole migration mechanism, ultraviolet photoelectron spectroscopy (UPS) measurements were performed on ZnO and ZnO@Ag samples (Figures 4A and 4B). The UPS spectra reveal a work function of 3.98 eV for ZnO and 4.12 eV for ZnO@Ag, indicating an increase upon Ag loading. This increase in work function upon Ag loading suggested a shift in the electronic structure, consistent with the formation of a heterojunction between ZnO and Ag. The difference in energy levels facilitates electron migration from the ZnO conduction band to the Ag nanoparticles, supporting enhanced electron-hole separation. In particular, the shift in the secondary electron cutoff from 17.24 eV for ZnO to 17.1 eV for ZnO@Ag provided direct evidence of electronic interactions between ZnO and ZnO@Ag, which aligned with our proposed mechanism of charge transfer enhancement. The schematic diagram (Figure 4C) visually represented the electron and hole migration mechanism between ZnO and Ag nanoparticles. The diagram included the energies of the conduction band (LUMO) and valence band (HOMO) for ZnO, valence band (VB) edge energy were confirmed by the formulation of VB = CB + Eg as previously reported,[41] as well as the Fermi level for Ag nanoparticles, illustrating the charge transfer dynamics. This help clarify the role of Ag in capturing electrons from the conduction band of ZnO, thereby enhancing charge separation and promoting ROS generation.

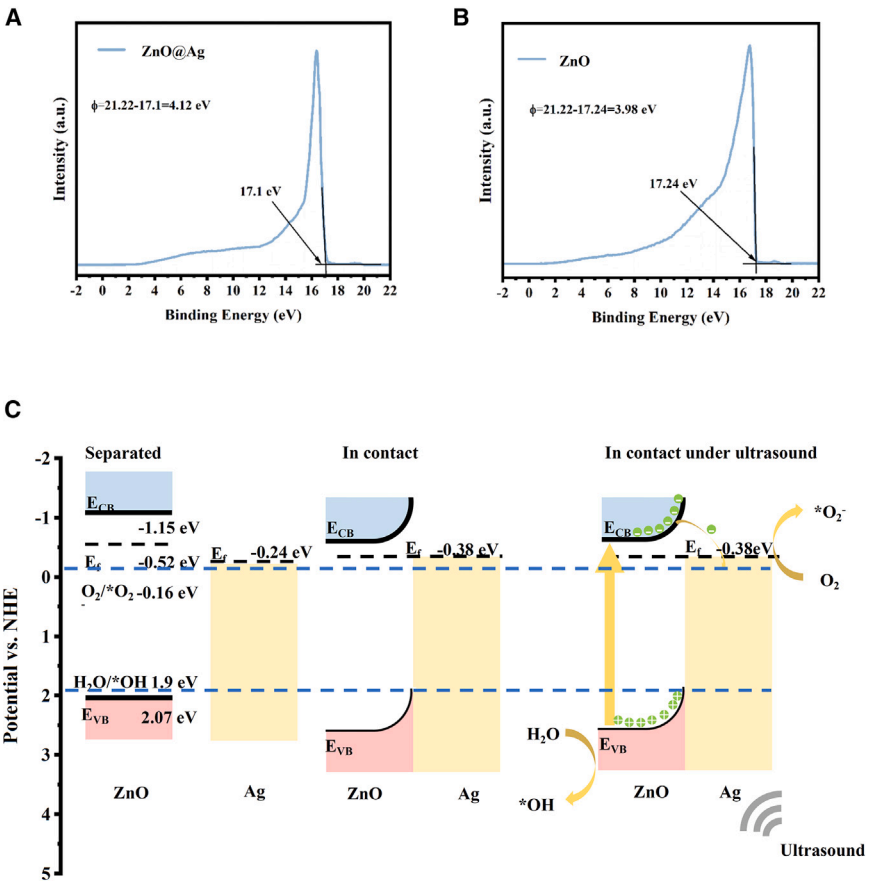

Figure 4. The electron/hole migration mechanism for ZnO@Ag

(A) The UPS result for ZnO@Ag sample.

(B) The UPS result for ZnO sample.

(C) The schematic diagram for illustrating the electron and hole migration mechanism between ZnO and Ag nanoparticles.

The biosafety and anti-tumor effect of ZnO and ZnO@Ag NRs *in vitro*

We initially evaluated the biosafety of ZnO and ZnO@Ag NRs in CT-26 cells using Cell Counting Kit-8 (CCK8) assays. The results showed that 83% of CT-26 cells survived ZnO@Ag treatment till a concentration of 25 μg/mL, demonstrating the NRs' good biocompatibility (Figure 5A). The ZnO@Ag group had the most effective cell-killing effects under ultrasound (1.5 W/cm^2, 50% duty cycle, 1 MHz, 5 min) than any of the other five groups (Figure 5B). Calcein-AM (live cells) and propidium iodide (PI) staining confirmed the biosafety and antitumor effects of both NRs. (Figure 5C). Minimal red fluorescence was observed in PBS with or without US treatment, indicating SDT's biosafety. Additionally, minimal red fluorescence and widespread green fluorescence in the ZnO and ZnO@Ag groups without US treatment confirmed the high biosafety of both NRs. With US exposure (1.5 W/cm^2, 50% duty cycle, 1 MHz, 5 min), the ZnO@Ag group displayed stronger red fluorescence compared to the ZnO group, indicating that ZnO@Ag could stimulate more cancer cell death than ZnO. To investigate the cell-killing mechanisms of both NRs as sonosensitizers and chemodynamic agents, we used 2′, 7′- diacetate of dichlorofluorescein (DCFH-DA), which turns into green-fluorescent DCF upon oxidation by ROS, to evaluate intracellular ROS levels (Figure 5D). Under ultrasound irradiation, ROS levels were significantly higher in ZnO@Ag than in ZnO, possibly due to the enhanced electronic band structure of ZnO@Ag.

The cells were stained with Annexin V-FITC/PI and counted via flow cytometry; the results revealed that while the ZnO + US group showed a cancer apoptosis rate of 19.1%, the highest rate was in the ZnO@Ag + US group at 51.4%, underscoring its potential in ultrasound irradiation (Figure 6A). Meanwhile, no significant cell apoptosis was observed in the other four groups, indicating the biosafety of ZnO, ZnO@Ag, and the ultrasound irradiation. We also assessed mitochondrial damage using JC-1 dye, where red fluorescence indicated healthy mitochondria and green fluorescence indicated damaged mitochondria. The results, shown in Figure 6B, indicated severe mitochondrial damage in both the ZnO + US group and the ZnO@Ag + US group, as evidenced by strong green fluorescence. Additionally, the strongest green fluorescence in the ZnO@Ag + US group suggested an enhanced antitumor effect compared to ZnO, consistent with previous findings. Correspondingly, the strong red fluorescence confirmed the biosafety of ZnO, ZnO@Ag, and ultrasound irradiation.

Additionally, the pathogen represented by *Fusobacterium nucleatum*, known to significantly promote the progression of colorectal cancer,[42] could be inhibited by the ROS generated during US treatment with the NRs. This inhibition might benefit the outcome of colorectal cancer, particularly in cases associated with bacterial infections infected.[43,44] We then assessed the antibacterial efficacy of ZnO and ZnO@Ag NRs using the spread plate method. *F. nucleatum* at a concentration of 2 × 10^8 CFU/mL was mixed with ZnO and ZnO@Ag; the mixture was then subjected to US exposure (1.5 W/cm^2, 50% duty cycle, 1 MHz, 5 min) or was left untreated. As shown in Figure 7A, minimal antibacterial effects were observed in the PBS group, ZnO group, ZnO@Ag group, and PBS + US group. In contrast, the ZnO + US group and ZnO@Ag + US group displayed antibacterial effects, with antibacterial efficiencies of 85.78% and 96.21%, respectively. Subsequent statistical chart further confirmed this trend (Figure 7B). From these results, it can be inferred that the antibacterial effect of ZnO@Ag was superior to that of ZnO, a performance aligned with increased ROS production.

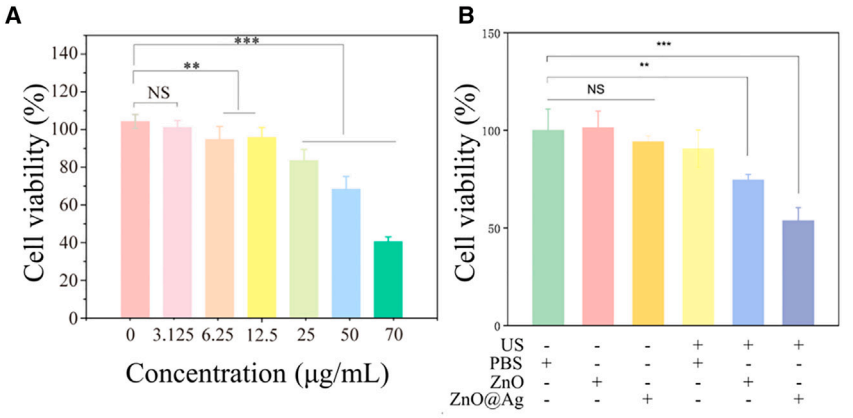

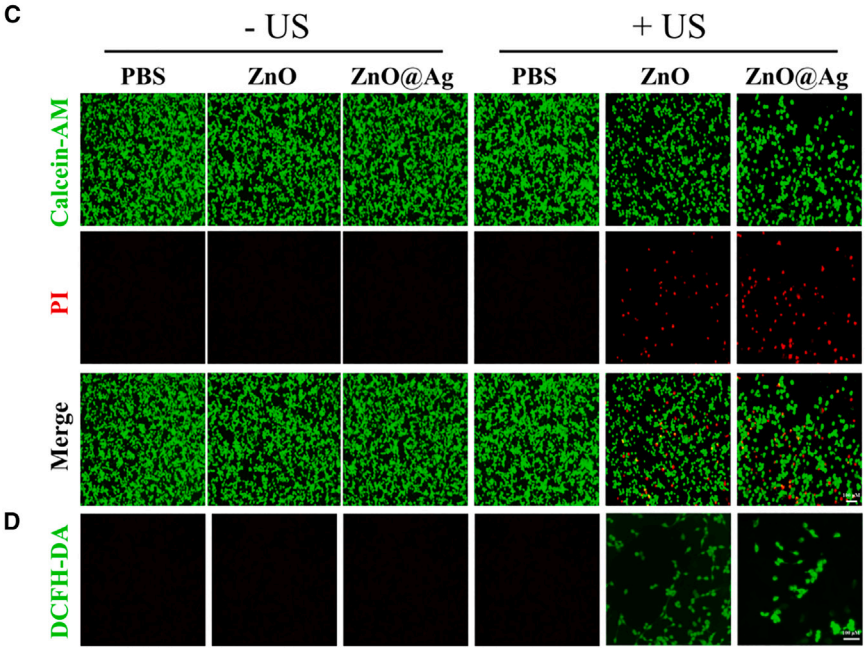

Figure 5. The biosafety and anti-tumor effect of ZnO and ZnO@Ag NRs *in vitro*

(A) The biosafety of ZnO and ZnO@Ag NRs in CT-26 cells.

(B) The anti-tumor effect of ZnO and ZnO@Ag NRs with or without US irradiation.

(C) The results of live and dead cell staining of ZnO and ZnO@Ag NRs with or without US irradiation. Scale bar, 100 μm.

(D) The evaluation of intracellular ROS levels in ZnO and ZnO@Ag NRs with or without US irradiation. Scale bar, 100 μm.

Data are represented as mean ± SD, "NS" means $p > 0.05$, "***" means $p < 0.01$, "****" means $p < 0.001$.

The biosafety and anti-tumor effect of ZnO and ZnO@Ag NRs *in vivo*

Based on the *in vitro* results, we conducted a comprehensive *in vivo* study using CT26 tumor-bearing BALB/c mice and ZnO@Ag and ZnO NRs. We established a subcutaneous tumor model in 5-week-old male Balb/c mice (20–25g), administering treatments via tail vein injection to evaluate the anti-tumor effects of ZnO@Ag. After tumors reached approximately 100 mm^3, we randomly divided 40 mice into six groups (PBS, ZnO, ZnO@Ag, PBS + US, ZnO + US, ZnO@Ag + US), each group containing five mice. A NRs treatment (2 mg/kg for ZnO or ZnO@Ag) was administered intravenously on days 0 and 2. An ultrasound intervention (1.5 W/cm^2, 50% duty cycle, 1 MHz, 15 min) was conducted on days 1 and 3 for two weeks, weight and tumor volume were measured bi-daily (Figure 8A). Results show that the PBS group, ZnO group, and ZnO@Ag group had unrestricted tumor growth, highlighting their limited intrinsic anti-tumor properties (Figure 8B). However, therapeutic outcomes improved significantly following US intervention; notably, the ZnO@Ag + US group demonstrated the most substantial effect with a significant reduction in tumor volume (Figures 8C and 8E). Additionally, mouse body weight remained stable throughout the treatment period (Figure 8D), underscoring the treatment's safety and indicating that neither ZnO@Ag nor ZnO NRs, nor ultrasound exposure, induced systemic toxicity or adversely affected the mice. The enhanced anti-tumor efficacy of ZnO@Ag compared to ZnO was potentially attributed to the unique electronic band structure boosting SDT performance following Ag loading. To validate the therapeutic efficacy, we stained histological sections with Hematoxylin & Eosin (H&E), Terminal deoxynucleotidyl transferase dUTP nick end labeling (TUNEL), and Ki-67. The results indicated that tumor cell structures remained largely intact in the PBS, ZnO, ZnO@Ag, and PBS + US groups, while both the ZnO@Ag + US and ZnO + US groups exhibited varying degrees of necrosis. The ZnO@Ag + US group showed the most severe tumor tissue damage and the largest area of necrosis compared to the ZnO + US group (Figure 9A). Cellular proliferation post-intervention was assessed using Ki-67 immunohistochemical staining on tumor sections. Extensive cell proliferation was observed in the PBS group, while ZnO@Ag significantly inhibited tumor cell proliferation, consistent with earlier tumor growth curve findings. Major organs were collected and stained with Hematoxylin and Eosin (H&E). None of the intervention groups showed significant organ toxicity (Figure 9B). These results confirm the biocompatibility and safety of the treatments, particularly for ZnO@Ag NRs used with ultrasound under the tested conditions. This comprehensive study underscores the potential of ZnO@Ag NRs as a potent cancer treatment strategy when combined with ultrasound.

DISCUSSION

In this study, we successfully synthesized and characterized a novel nanocomposite, ZnO@Ag NRs, which significantly

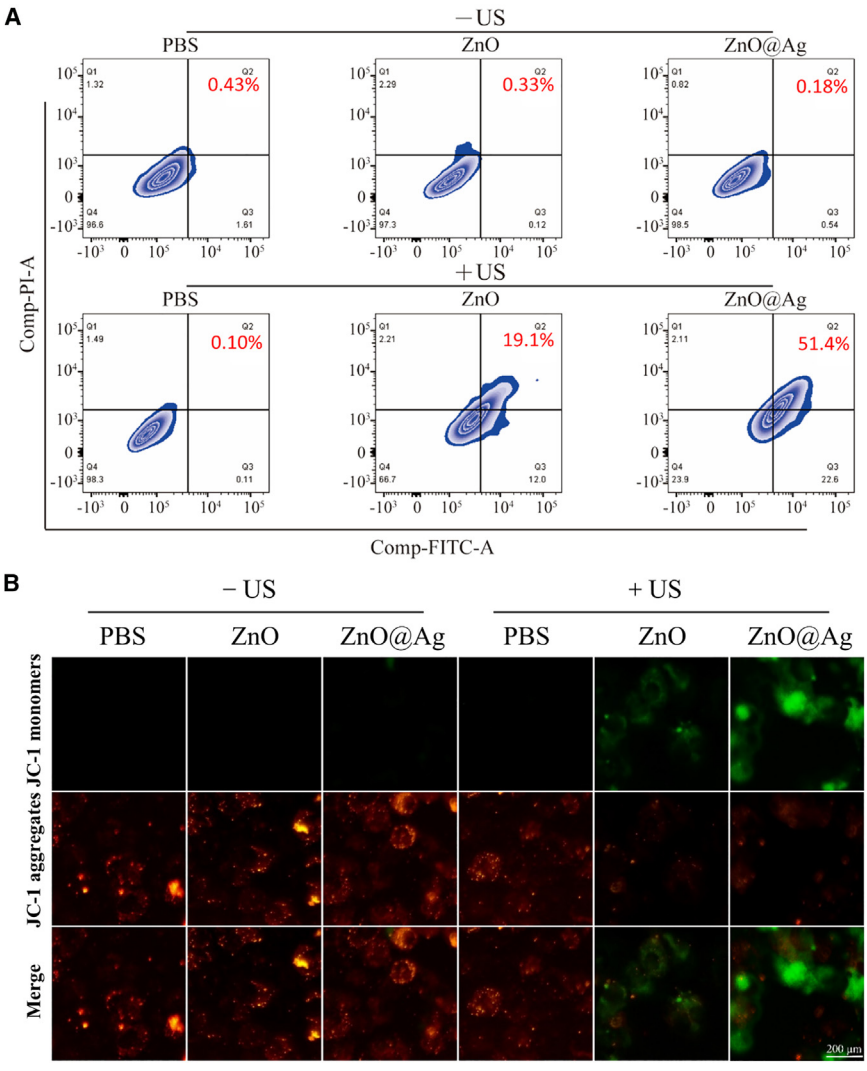

Figure 6. The anti-tumor effect of ZnO and ZnO@Ag NRs *in vitro*

(A) The flow cytometry results of Annexin V-FITC/PI-stained CT-26 cells co-culture with ZnO and ZnO@Ag NRs undergoing US irradiation or not.

(B) The result for mitochondrial damage of CT-26 cells co-culture with ZnO and ZnO@Ag NRs undergoing US irradiation or not. Scale bar, 200 μm.

enhances the efficacy of SDT for cancer treatment. The incorporation of silver nanoparticles (AgNPs) into ZnO NRs not only improved the generation of ROS under US irradiation but also demonstrated a notable increase in tumor cell cytotoxicity both *in vitro* and *in vivo*.

The enhanced ROS generation observed in ZnO@Ag NRs can be attributed to the formation of a heterojunction between ZnO and Ag, which facilitates efficient electron-hole separation.[45] This heterojunction arises due to the difference in their Fermi levels, allowing for a smooth transfer of electrons from ZnO to AgNPs. The Ag nanoparticles, acting as electron sinks, effectively capture electrons and prevent their recombination with holes, thereby prolonging the lifetime of charge carriers and promoting higher ROS generation.[46] This enhanced ROS generation involves the band structure of the ZnO@Ag NRs. The Ag nanoparticles modify the electronic properties of the ZnO nanorods, creating more active sites for ROS production.[47] This is crucial because ROS play a key role in damaging cellular components such as DNA, proteins, and lipids, leading to cell apoptosis. Additionally, the presence of Ag nanoparticles can enhance light absorption and charge separation efficiency, further boosting ROS production.[48] This separation allows more holes to participate in the oxidation reactions that generate ROS. Even a sparse distribution of AgNPs significantly impacts electron-hole separation due to their high electron affinity. Previous studies have shown that low concentrations of noble metal nanoparticles can effectively enhance the photocatalytic and sonodynamic properties of semiconductor materials by improving charge separation efficiency.[49,50] Our findings, confirmed through ESR and UV-vis spectroscopy, demonstrate that ZnO@Ag NRs generate significantly higher levels of singlet oxygen ($^1O_2$) and hydroxyl radicals (·OH) compared to ZnO NRs alone under identical ultrasound conditions. The enhanced ROS generation observed in ZnO@Ag NRs, including singlet oxygen, was confirmed through ESR spectroscopy using the TEMP probe. TEMP reacts specifically with $^1O_2$ to form TEMP-$^1O_2$, generating a distinct triplet signal, which is a well-established method for singlet oxygen detection in SDT studies.[12,31] While the ABDA assay is more common in photodynamic therapy, the TEMP-based ESR method provides direct confirmation of $^1O_2$ generation under ultrasound, making it highly suitable for our SDT study. This enhanced $^1O_2$ production is a result of the effective electron-hole separation facilitated by the ZnO@Ag heterojunction, which promotes efficient ROS generation.

While AgNPs typically exhibit a surface plasmon resonance (SPR) band around 400–420 nm, this characteristic band was not observed in our composite material. This absence can be attributed to several factors. Firstly, the very small and uniformly dispersed AgNPs on ZnO NRs can cause broadening and a shift in the SPR band. When AgNPs are very small (typically less than 10 nm), the SPR band can become less pronounced or undetectable due to increased damping of the plasmon resonance.[47,51] Secondly, the strong interaction and charge transfer between AgNPs and ZnO NRs can lead to quenching or significant modification of the SPR band.[52] Lastly, the low concentration of AgNPs relative to ZnO NRs might contribute to the weak or undetectable SPR band.[53] Additionally, the presence of ZnO NRs

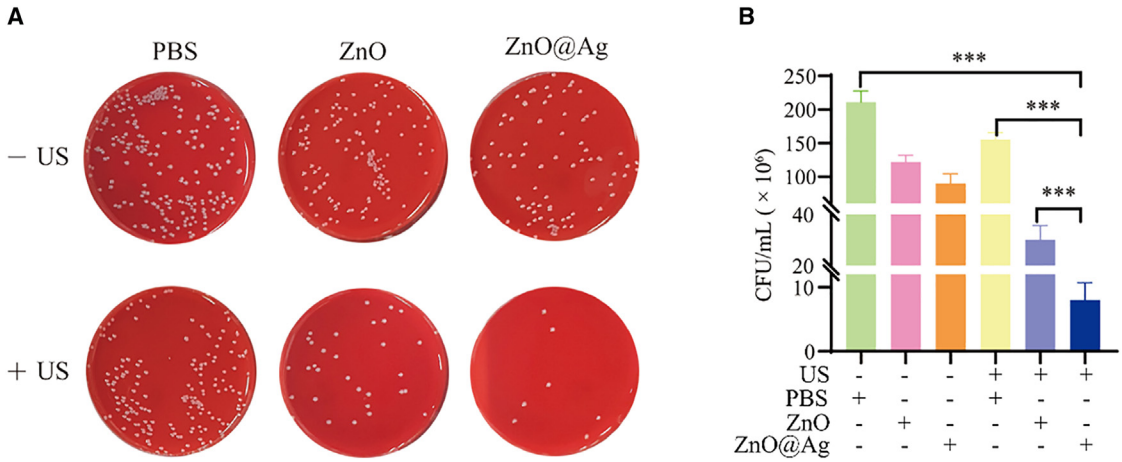

Figure 7. The antibacterial effect of ZnO and ZnO@Ag NRs *in vitro*

(A) The representative image of plate in all groups.

(B) The statistical result for the evaluation of antibacterial effect in all groups. Data are represented as mean ± SD, "****" means $p < 0.001$.

and other components in the sample matrix can cause scattering and absorption that overlap with or mask the SPR band of AgNPs.[54]

In vitro studies revealed that ZnO@Ag NRs exhibit excellent biocompatibility up to a concentration of 25 μg/mL, with minimal cytotoxicity observed in the absence of US. Upon US irradiation, ZnO@Ag NRs showed significantly enhanced cell-killing effects compared to ZnO NRs. This enhanced efficacy was further validated through live/dead cell staining, intracellular ROS measurement, and flow cytometry analysis, indicating that ZnO@Ag NRs could effectively induce apoptosis in cancer cells. The Ag nanoparticles modify the electronic properties of the ZnO nanorods, creating more active sites for ROS production.[45,53] This is crucial because ROS play a key role in damaging cellular components such as DNA, proteins, and lipids, leading to cell apoptosis.[55,56] Additionally, the presence of Ag nanoparticles can enhance light absorption and charge separation efficiency, further boosting ROS production.[45]

ZnO@Ag NRs cause significant mitochondrial damage, evidenced by strong green fluorescence from JC-1 staining. The mechanism involves ROS generation, which induces oxidative stress, leading to lipid peroxidation of mitochondrial membranes and loss of mitochondrial membrane potential.[57] This disruption impairs the electron transport chain, reducing ATP production and initiating apoptosis pathways. The release of cytochrome C from damaged mitochondria into the cytoplasm activates caspases, which execute apoptosis.[58]

The *in vivo* studies in CT26 tumor-bearing BALB/c mice demonstrated that ZnO@Ag NRs, when combined with US, significantly inhibited tumor growth without causing systemic toxicity. The stable body weights of treated mice and the absence of significant histopathological changes in major organs confirmed the biosafety of the treatment. Histological analysis of tumor tissues showed extensive necrosis and reduced cell proliferation in the ZnO@Ag + US group, highlighting the potent anti-tumor efficacy of this treatment modality.

An additional advantage of ZnO@Ag NRs is their intrinsic antibacterial properties, which are beneficial for treating cancers associated with bacterial infections. The superior antibacterial efficacy of ZnO@Ag NRs compared to ZnO NRs alone is attributed to the synergistic effect of ROS generation and the intrinsic antibacterial activity of AgNPs.[59,60]

In conclusion, our study demonstrates that ZnO@Ag NRs are a potent and safe sonosensitizer for cancer therapy, capable of significantly enhancing ROS generation under US and effectively inducing tumor cell death. Their dual functionality, including antibacterial properties and antitumor effect, further expands their therapeutic potential. Our findings suggest that the unique heterostructure of ZnO@Ag NRs facilitates efficient electron-hole separation, thereby preventing the recombination of charge carriers and enhancing the production of cytotoxic ROS. This mechanism is pivotal for the observed increase in anticancer efficacy, which is complemented by the material's good biocompatibility and additional antibacterial properties. The dual functionality of ZnO@Ag NRs underscores their potential as a versatile tool in cancer treatment, particularly in cases associated with bacterial infections. Future work will focus on optimizing the nanoparticle synthesis for scalable production and further clinical evaluation to explore the full potential of this promising SDT agent. It contributes significantly to the growing field of nanomedicine by advancing the design and application of functionally enhanced nanomaterials, exposing cancer patients to safer and more effective therapeutic options.

Limitations of the study

Future research focused on mechanistic insights, scalability, and clinical translation will be key to realizing the full potential of ZnO@Ag NRs in cancer treatment. Additionally, understanding the interaction between ZnO@Ag NRs and the tumor microenvironment could provide new avenues for optimizing therapeutic strategies. The promising results from this study lay a solid

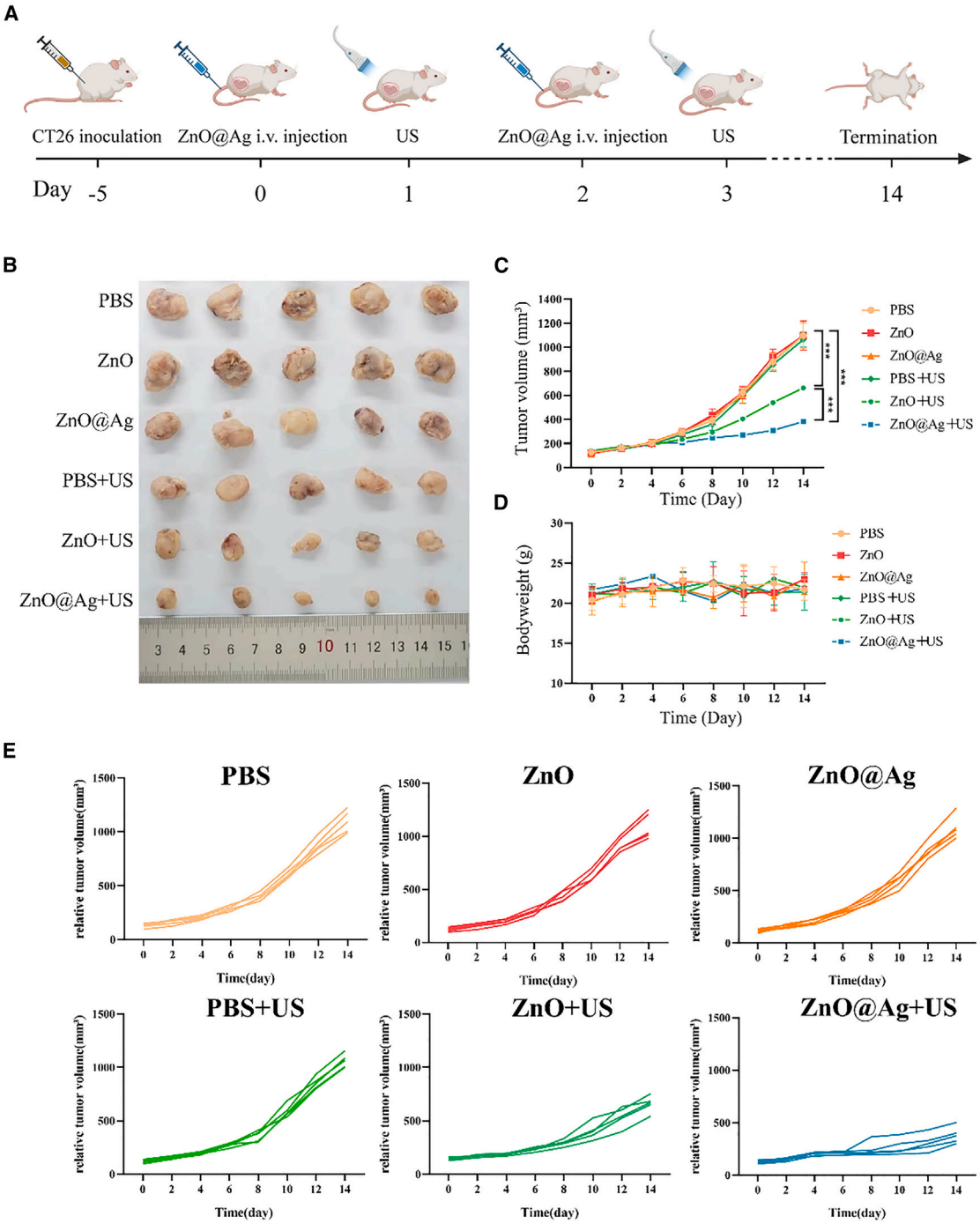

Figure 8. The anti-tumor effect of ZnO and ZnO@Ag NRs *in vivo*

(A) Schematic of the NRs treatment strategy.

(B) The digital image of the tumors in all groups.

(C) The results of tumor volume in all groups during the intervention.

(D) The results of mice bodyweight in all groups during the intervention.

(E) The changes of tumor volume for every individual mouse in all groups during the intervention.

Data are represented as mean ± SD, "****" means $p < 0.001$.

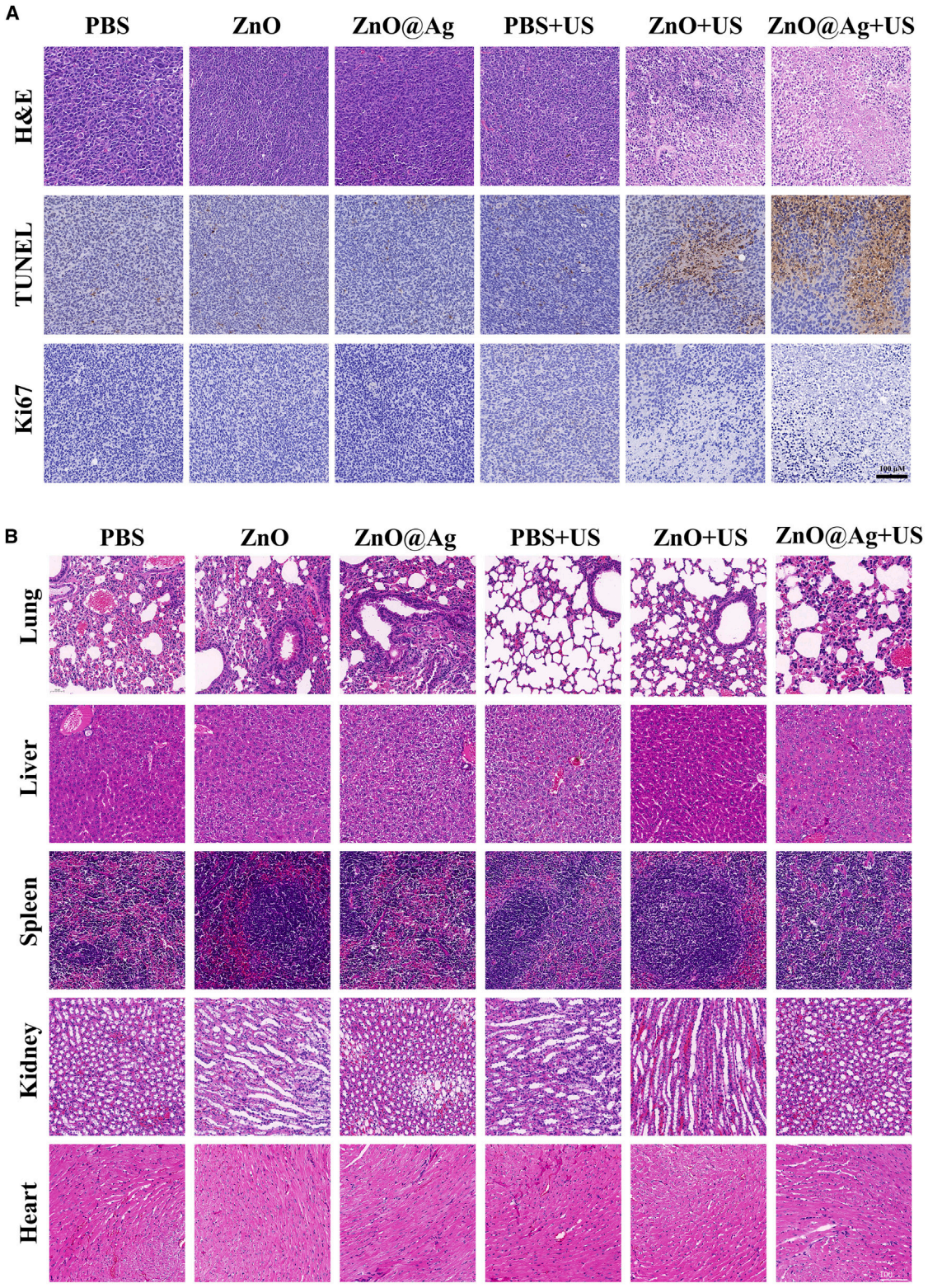

Figure 9. The biosafety and anti-tumor results of ZnO and ZnO@Ag NRs *in vivo*

(A) The H&E, TUNEL, Ki67 results for tumor sections in all groups. Scale bar, 100 μm.

(B) The H&E results for major organs (including lung, liver, spleen, kidney, and heart) in all groups. Scale bar, 100 μm.

foundation for the development of ZnO@Ag NRs as a versatile platform for cancer therapy, opening up new possibilities for combining nanotechnology with traditional treatment modalities to achieve better clinical outcomes.

RESOURCE AVAILABILITY

Lead contact

Further information and requests for resources could be directed to and will be fulfilled by the lead contact, Yefei Zhu (yefei_zhu@foxmail.com).

Materials availability

The authors confirm that the materials are available from the lead contact, Y.Z. (yefei_zhu@foxmail.com), upon reasonable request.

Data and code availability

- All data reported in this paper will be shared by the lead contact upon request.
- This paper does not report the original code.
- Any additional information required to re-analyze the data reported in this paper is available from the lead contact upon reasonable request.

ACKNOWLEDGMENTS

We thank Biorender (https://www.biorender.com) for the technical support provided in the schematic drawing. We thank the supporting of the National Natural Science Foundation of China (NO. 82102252, 82330093), Research Fund of Shanghai University of Medicine & Health Sciences (SSF-22-25-001), and Research Fund of Shanghai Jinshan District Health Commission (JSKJ-KTMS-2022-15).

AUTHOR CONTRIBUTIONS

Y.T., writing - original draft, conceptualization, data curation, formal analysis, investigation, methodology, validation; W.F., data curation, investigation, writing and editing, funding acquisition; W.Z., writing - original draft, conceptualization, data curation, formal analysis, investigation, methodology, validation; L.Z., methodology, validation, funding acquisition; L.F., conceptualization, supervision, review and editing; H.Q., conceptualization, supervision, review and editing, funding acquisition; Y.Z., review and editing, conceptualization, supervision, data curation, investigation, methodology, validation.

DECLARATION OF INTERESTS

The authors declare no competing interests.

STAR★METHODS

Detailed methods are provided in the online version of this paper and include the following:

- KEY RESOURCES TABLE
- EXPERIMENTAL MODE AND STUDY PARTICIPANT DETAILS
  - Materials
  - Cell line
  - Animals
- METHOD DETAILS
  - Synthesis of nanoparticles
  - Characterization of nanoparticles
  - In vitro biosafety evaluation and antitumor efficacy
  - In vivo antitumor efficacy
- QUANTIFICATION AND STATISTICAL ANALYSIS
- ADDITIONAL RESOURCES

SUPPLEMENTAL INFORMATION

Supplemental information can be found online at https://doi.org/10.1016/j.isci.2025.111858.

Received: May 5, 2024
Revised: August 22, 2024
Accepted: January 17, 2025
Published: January 27, 2025

REFERENCES

1. Gao, P., Pan, W., Li, N., and Tang, B. (2019). Fluorescent probes for organelle-targeted bioactive species imaging. Chem. Sci. *10*, 6035–6071. https://doi.org/10.1039/c9sc01652j.
2. Zhang, C., Wang, X., Du, J., Gu, Z., and Zhao, Y. (2021). Reactive Oxygen Species-Regulating Strategies Based on Nanomaterials for Disease Treatment. Adv. Sci. *8*, 2002797. https://doi.org/10.1002/advs.202002797.
3. Anglada, J.M., Martins-Costa, M., Francisco, J.S., and Ruiz-López, M.F. (2015). Interconnection of reactive oxygen species chemistry across the interfaces of atmospheric, environmental, and biological processes. Acc. Chem. Res. *48*, 575–583. https://doi.org/10.1021/ar500412p.
4. Nosaka, Y., and Nosaka, A.Y. (2017). Generation and Detection of Reactive Oxygen Species in Photocatalysis. Chem. Rev. *117*, 11302–11336. https://doi.org/10.1021/acs.chemrev.7b00161.
5. Zhu, Y., Zhu, R., Xi, Y., Zhu, J., Zhu, G., and He, H. (2019). Strategies for enhancing the heterogeneous Fenton catalytic reactivity: A review. Appl. Catal. B Environ. *255*, 117739.
6. Cao, S., Zhao, Z., Zheng, Y., Wu, Z., Ma, T., Zhu, B., Yang, C., Xiang, X., Ma, L., Han, X., et al. (2022). A Library of ROS-Catalytic Metalloenzyme Mimics with Atomic Metal Centers. Adv. Mater. *34*, e2200255. https://doi.org/10.1002/adma.202200255.
7. Ziwei, K., Yasotha, B., Zhoufeng, K., and Sibudjing, M. (2016). Design of highly stable and selective core/yolk-shell nanocatalysts-A review. Appl. Catal. B Environ. *188*, 324–341.
8. Peer, D., Karp, J.M., Hong, S., Farokhzad, O.C., Margalit, R., and Langer, R. (2007). Nanocarriers as an emerging platform for cancer therapy. Nat. Nanotechnol. *2*, 751–760. https://doi.org/10.1038/nnano.2007.387.
9. Wang, X.Q., Wang, W., Peng, M., and Zhang, X.Z. (2021). Free radicals for cancer theranostics. Biomaterials *266*, 120474. https://doi.org/10.1016/j.biomaterials.2020.120474.
10. Zhang, D., Meng, Y., Song, Y., Cui, P., Hu, Z., and Zheng, X. (2022). Precision therapy through breaking the intracellular redox balance with an MOF-based hydrogel intelligent nanobot for enhancing ferroptosis and activating immunotherapy. Nanoscale *14*, 8441–8453. https://doi.org/10.1039/d2nr00950a.
11. Hu, H., Zhao, J., Ma, K., Wang, J., Wang, X., Mao, T., Xiang, C., Luo, H., Cheng, Y., Yu, M., et al. (2023). Sonodynamic therapy combined with phototherapy: Novel synergistic strategy with superior efficacy for antitumor and antiinfection therapy. J. Contr. Release *359*, 188–205. https://doi.org/10.1016/j.jconrel.2023.05.041.
12. Pan, X., Wang, H., Wang, S., Sun, X., Wang, L., Wang, W., Shen, H., and Liu, H. (2018). Sonodynamic therapy (SDT): a novel strategy for cancer nanotheranostics. Science China. Life Sci. *61*, 415–426. https://doi.org/10.1007/s11427-017-9262-x.
13. Bai, S., Yang, N., Wang, X., Gong, F., Dong, Z., Gong, Y., Liu, Z., and Cheng, L. (2020). Ultrasmall Iron-Doped Titanium Oxide Nanodots for Enhanced Sonodynamic and Chemodynamic Cancer Therapy. ACS Nano *14*, 15119–15130. https://doi.org/10.1021/acsnano.0c05235.
14. Chen, P., Zhang, P., Shah, N.H., Cui, Y., and Wang, Y. (2023). A Comprehensive Review of Inorganic Sonosensitizers for Sonodynamic Therapy. Int. J. Mol. Sci. *24*, 12001.

15. Liu, X., Pan, X., Wang, C., and Liu, H. (2023). Modulation of reactive oxygen species to enhance sonodynamic therapy. Particuology *75*, 199–216. https://doi.org/10.1016/j.partic.2022.08.001.

16. Li, D., Yang, Y., Li, D., Pan, J., Chu, C., and Liu, G. (2021). Organic Sonosensitizers for Sonodynamic Therapy: From Small Molecules and Nanoparticles toward Clinical Development. Small *17*, e2101976. https://doi.org/10.1002/smll.202101976.

17. Sun, L., Wang, P., Zhang, J., Sun, Y., Sun, S., Xu, M., Zhang, L., Wang, S., Liang, X., and Cui, L. (2021). Design and application of inorganic nanoparticles for sonodynamic cancer therapy. Biomater. Sci. *9*, 1945–1960. https://doi.org/10.1039/d0bm01875a.

18. Zhao, L.-Y., Mei, J.-X., Yu, G., Lei, L., Zhang, W.-H., Liu, K., Chen, X.-L., Kołat, D., Yang, K., and Hu, J.-K. (2023). Role of the gut microbiota in anticancer therapy: from molecular mechanisms to clinical applications. Signal Transduct. Targeted Ther. *8*, 201. https://doi.org/10.1038/s41392-023-01406-7.

19. Endo, S., Kudo, N., Yamaguchi, S., Sumiyoshi, K., Motegi, H., Kobayashi, H., Terasaka, S., and Houkin, K. (2015). Porphyrin derivatives-mediated sonodynamic therapy for malignant gliomas *in vitro*. Ultrasound Med. Biol. *41*, 2458–2465. https://doi.org/10.1016/j.ultrasmedbio.2015.05.007.

20. Canavese, G., Ancona, A., Racca, L., Canta, M., Dumontel, B., Barbaresco, F., Limongi, T., and Cauda, V. (2018). Nanoparticle-assisted ultrasound: A special focus on sonodynamic therapy against cancer. Chem. Eng. J. *340*, 155–172. https://doi.org/10.1016/j.cej.2018.01.060.

21. Byun, K.T., Kim, K.Y., and Kwak, H.Y. (2005). Sonoluminescence characteristics from micron and submicron bubbles. J. Kor. Phys. Soc. *47*, 1010–1022.

22. Costley, D., Mc Ewan, C., Fowley, C., McHale, A.P., Atchison, J., Nomikou, N., and Callan, J.F. (2015). Treating cancer with sonodynamic therapy: a review. Int. J. Hyperther. *31*, 107–117. https://doi.org/10.3109/02656736.2014.992484.

23. Wu, J., Huang, Y., Ye, W., and Li, Y. (2017). CO(2) Reduction: From the Electrochemical to Photochemical Approach. Adv. Sci. *4*, 1700194. https://doi.org/10.1002/advs.201700194.

24. Haldar, R., Jakoby, M., Mazel, A., Zhang, Q., Welle, A., Mohamed, T., Krolla, P., Wenzel, W., Diring, S., Odobel, F., et al. (2018). Anisotropic energy transfer in crystalline chromophore assemblies. Nat. Commun. *9*, 4332. https://doi.org/10.1038/s41467-018-06829-3.

25. Pan, X., Bai, L., Wang, H., Wu, Q., Wang, H., Liu, S., Xu, B., Shi, X., and Liu, H. (2018). Metal-Organic-Framework-Derived Carbon Nanostructure Augmented Sonodynamic Cancer Therapy. Adv. Mater. *30*, e1800180. https://doi.org/10.1002/adma.201800180.

26. Liang, S., Deng, X., Ma, P., Cheng, Z., and Lin, J. (2020). Recent Advances in Nanomaterial-Assisted Combinational Sonodynamic Cancer Therapy. Adv. Mater. *32*, e2003214. https://doi.org/10.1002/adma.202003214.

27. Li, Y., Zhou, H., Chen, Y., Zhao, Y., and Zhu, H. (2020). Efficient hot-electron extraction in two-dimensional semiconductor heterostructures by ultrafast resonant transfer. J. Chem. Phys. *153*, 044705. https://doi.org/10.1063/5.0018072.

28. Zheng, S.W., Wang, H.Y., Wang, L., Wang, H., and Sun, H.B. (2020). Layer-Dependent Electron Transfer and Recombination Processes in MoS(2)/WSe(2) Multilayer Heterostructures. J. Phys. Chem. Lett. *11*, 9649–9655. https://doi.org/10.1021/acs.jpclett.0c02952.

29. Park, T.G., Choi, B.K., Park, J., Kim, J., Chang, Y.J., and Rotermund, F. (2021). Interlayer Coupling and Ultrafast Hot Electron Transfer Dynamics in Metallic VSe(2)/Graphene van der Waals Heterostructures. ACS Nano *15*, 7756–7764. https://doi.org/10.1021/acsnano.1c01723.

30. Hussain, M.Z., Schneemann, A., Fischer, R.A., Zhu, Y., and Xia, Y. (2018). MOF Derived Porous ZnO/C Nanocomposites for Efficient Dye Photodegradation. ACS Appl. Energy Mater. *1*, 4695–4707. https://doi.org/10.1021/acsaem.8b00822.

31. Xu, T., Zhao, S., Lin, C., Zheng, X., and Lan, M. (2020). Recent advances in nanomaterials for sonodynamic therapy. Nano Res. *13*, 2898–2908. https://doi.org/10.1007/s12274-020-2992-5.

32. Zhao, L., Zhang, Y., Wang, F., Hu, S., Wang, X., Ma, B., Liu, H., Lin Wang, Z., and Sang, Y. (2017). BaTiO3 nanocrystal-mediated micro pseudo-electrochemical cells with ultrasound-driven piezotronic enhancement for polymerization. Nano Energy *39*, 461–469. https://doi.org/10.1016/j.nanoen.2017.07.037.

33. Maggard, P.A. (2021). Capturing Metastable Oxide Semiconductors for Applications in Solar Energy Conversion. Acc. Chem. Res. *54*, 3160–3171. https://doi.org/10.1021/acs.accounts.1c00210.

34. Younis, A., Lin, C.H., Guan, X., Shahrokhi, S., Huang, C.Y., Wang, Y., He, T., Singh, S., Hu, L., Retamal, J.R.D., et al. (2021). Halide Perovskites: A New Era of Solution-Processed Electronics. Adv. Mater. *33*, e2005000. https://doi.org/10.1002/adma.202005000.

35. Warren, R., Privitera, A., Kaienburg, P., Lauritzen, A.E., Thimm, O., Nelson, J., and Riede, M.K. (2019). Controlling energy levels and Fermi level en route to fully tailored energetics in organic semiconductors. Nat. Commun. *10*, 5538. https://doi.org/10.1038/s41467-019-13563-x.

36. He, F., Li, W., Liu, B., Zhong, Y., Jin, Q., and Qin, X. (2024). Progress of Piezoelectric Semiconductor Nanomaterials in Sonodynamic Cancer Therapy. ACS Biomater. Sci. Eng. *10*, 298–312. https://doi.org/10.1021/acsbiomaterials.3c01232.

37. Liu, Y., Wang, Y., Zhen, W., Wang, Y., Zhang, S., Zhao, Y., Song, S., Wu, Z., and Zhang, H. (2020). Defect modified zinc oxide with augmenting sonodynamic reactive oxygen species generation. Biomaterials *251*, 120075. https://doi.org/10.1016/j.biomaterials.2020.120075.

38. Rutherford, D., Remes, Z., Kolarova, K., Matolinova, I., Cech, J., Micova, J., and Rezek, B. (2024). Enhanced antimicrobial and photocatalytic effects of plasma-treated gallium-doped zinc oxide. Appl. Surf. Sci. *655*, 159567. https://doi.org/10.1016/j.apsusc.2024.159567.

39. Oualid, H.A., Amadine, O., Essamlali, Y., Kadmiri, I.M., El Arroussi, H., and Zahouily, M. (2019). Highly efficient catalytic/sonocatalytic reduction of 4-nitrophenol and antibacterial activity through a bifunctional Ag/ZnO nanohybrid material prepared via a sodium alginate method. Nanoscale Adv. *1*, 3151–3163. https://doi.org/10.1039/c9na00075e.

40. Gowthaman, N.S.K., Chen, J.-W., Dee, C.F., Chai, S.-P., and Chang, W.S. (2022). Nanostructural dimension and oxygen vacancy synergistically induced photoactivity across high surface area monodispersed AuNPs/ZnO nanorods heterojunction. J. Alloys Compd. *920*, 165836. https://doi.org/10.1016/j.jallcom.2022.165836.

41. Tan, J., Yu, M., Cai, Z., Lou, X., Wang, J., and Li, Z. (2021). MOF-derived synthesis of MnS/In(2)S(3)p-n heterojunctions with hierarchical structures for efficient photocatalytic CO(2) reduction. J. Colloid Interface Sci. *588*, 547–556. https://doi.org/10.1016/j.jcis.2020.12.110.

42. Kong, C., Yan, X., Zhu, Y., Zhu, H., Luo, Y., Liu, P., Ferrandon, S., Kalady, M.F., Gao, R., He, J., et al. (2021). Fusobacterium Nucleatum Promotes the Development of Colorectal Cancer by Activating a Cytochrome P450/Epoxyoctadecenoic Acid Axis via TLR4/Keap1/NRF2 Signaling. Cancer Res. *81*, 4485–4498. https://doi.org/10.1158/0008-5472.CAN-21-0453.

43. Jiang, H., Guo, Y., Yu, Z., Hu, P., and Shi, J. (2022). Nanocatalytic bacteria disintegration reverses immunosuppression of colorectal cancer. Natl. Sci. Rev. *9*, nwac169. https://doi.org/10.1093/nsr/nwac169.

44. Wang, X., Chen, Q., Zhu, Y., Wang, K., Chang, Y., Wu, X., Bao, W., Cao, T., Chen, H., Zhang, Y., and Qin, H. (2023). Destroying pathogen-tumor symbionts synergizing with catalytic therapy of colorectal cancer by biomimetic protein-supported single-atom nanozyme. Signal Transduct. Targeted Ther. *8*, 277. https://doi.org/10.1038/s41392-023-01491-8.

45. Jiang, X., He, W., Zhang, X., Wu, Y., Zhang, Q., Cao, G., Zhang, H., Zheng, J., Croley, T.R., and Yin, J.-J. (2018). Light-Induced Assembly of Metal Nanoparticles on ZnO Enhances the Generation of Charge Carriers, Reactive Oxygen Species, and Antibacterial Activity. J. Phys. Chem. C *122*, 29414–29425. https://doi.org/10.1021/acs.jpcc.8b10578.

46. Pang, X., Skillen, N., Bahnemann, D.W., Rooney, D.W., and Robertson, P.K.J. (2022). Photocatalytic H2O2 Generation Using Au-Ag Bimetallic Alloy Nanoparticles loaded on ZnO. Catalysts *12*, 939.

47. Kayani, Z.N., Manzoor, F., Zafar, A., Mahmood, M., Rasheed, M., and Anwar, M. (2020). Impact of Ag doping on structural, optical, morphological, optical and photoluminescent properties of ZnO nanoparticles. Opt. Quant. Electron. *52*, 344. https://doi.org/10.1007/s11082-020-02460-z.

48. Pimpliskar, P.V., Motekar, S.C., Umarji, G.G., Lee, W., and Arbuj, S.S. (2019). Synthesis of silver-loaded ZnO nanorods and their enhanced photocatalytic activity and photoconductivity study. Photochem. Photobiol. Sci. *18*, 1503–1511. https://doi.org/10.1039/C9PP00099B.

49. Chen, Q., Liang, C., Wang, C., and Liu, Z. (2015). An Imagable and Photothermal "Abraxane-Like" Nanodrug for Combination Cancer Therapy to Treat Subcutaneous and Metastatic Breast Tumors. Adv. Mater. *27*, 903–910. https://doi.org/10.1002/adma.201404308.

50. Vanlalhmingmawia, C., Lee, S.M., and Tiwari, D. (2023). Plasmonic noble metal doped titanium dioxide nanocomposites: Newer and exciting materials in the remediation of water contaminated with micropollutants. J. Water Proc. Eng. *51*, 103360. https://doi.org/10.1016/j.jwpe.2022.103360.

51. Jain, P.K., Huang, X., El-Sayed, I.H., and El-Sayed, M.A. (2008). Noble Metals on the Nanoscale: Optical and Photothermal Properties and Some Applications in Imaging, Sensing, Biology, and Medicine. Acc. Chem. Res. *41*, 1578–1586. https://doi.org/10.1021/ar7002804.

52. Link, S., and El-Sayed, M.A. (1999). Spectral Properties and Relaxation Dynamics of Surface Plasmon Electronic Oscillations in Gold and Silver Nanodots and Nanorods. J. Phys. Chem. B *103*, 8410–8426. https://doi.org/10.1021/jp9917648.

53. Wang, X., Ye, Q., Bai, L.-H., Su, X., Wang, T.-T., Peng, T.-W., Zhai, X.-Q., Huo, Y., Wu, H., Liu, C., et al. (2021). Enhanced UV Emission from ZnO on Silver Nanoparticle Arrays by the Surface Plasmon Resonance Effect. Nanoscale Res. Lett. *16*, 8. https://doi.org/10.1186/s11671-020-03470-2.

54. Kaidashev, V.E., Lyanguzov, N.V., Yuzyuk, Y.I., and Kaidashev, E.M. (2012). Amplification of raman scattering by localized plasmons in silver nanoparticles on the surface of zinc oxide nanorods. Tech. Phys. *57*, 1406–1410. https://doi.org/10.1134/S1063784212100088.

55. Guo, B., Yang, F., Zhang, L., Zhao, Q., Wang, W., Yin, L., Chen, D., Wang, M., Han, S., Xiao, H., and Xing, N. (2023). Cuproptosis Induced by ROS Responsive Nanoparticles with Elesclomol and Copper Combined with αPD-L1 for Enhanced Cancer Immunotherapy. Adv. Mater. *35*, e2212267. https://doi.org/10.1002/adma.202212267.

56. Wang, Y., Qi, H., Liu, Y., Duan, C., Liu, X., Xia, T., Chen, D., Piao, H.-L., and Liu, H.-X. (2021). The double-edged roles of ROS in cancer prevention and therapy. Theranostics *11*, 4839–4857. https://doi.org/10.7150/thno.56747.

57. Barrera, G., Gentile, F., Pizzimenti, S., Canuto, R.A., Daga, M., Arcaro, A., Cetrangolo, G.P., Lepore, A., Ferretti, C., Dianzani, C., and Muzio, G. (2016). Mitochondrial Dysfunction in Cancer and Neurodegenerative Diseases: Spotlight on Fatty Acid Oxidation and Lipoperoxidation Products. Antioxidants *5*, 7. https://doi.org/10.3390/antiox5010007.

58. Zhang, Y., Fang, Q., Wang, H., Qi, J., Sun, S., Liao, M., Wu, Y., Hu, Y., Jiang, P., Cheng, C., et al. (2023). Increased mitophagy protects cochlear hair cells from aminoglycoside-i nduced damage. Autophagy *19*, 75–91. https://doi.org/10.1080/15548627.2022.2062872.

59. Dhivya, S., Hussain, S.I., Jeya Sheela, S., and Kalaiselvam, S. (2019). Experimental study on microcapsules of Ag doped ZnO nanomaterials enhanced Oleic-Myristic acid eutectic PCM for thermal energy storage. Thermochim. Acta *671*, 70–82. https://doi.org/10.1016/j.tca.2018.11.010.

60. Lam, S.-M., Quek, J.-A., and Sin, J.-C. (2018). Mechanistic investigation of visible light responsive Ag/ZnO micro/nanoflowers for enhanced photocatalytic performance and antibacterial activity. J. Photochem. Photobiol. Chem. *353*, 171–184. https://doi.org/10.1016/j.jphotochem.2017.11.021.

STAR★METHODS

KEY RESOURCES TABLE

REAGENT or RESOURCE	SOURCE	IDENTIFIER
Bacterial strain		
Fusobacterium nucleatum	ATCC	ATCC25586
Chemicals, peptides, and recombinant proteins		
Zinc acetate dihydrate	Beyotime Biotechnology Co. LTD	Z433041-1kg/5970-45-6
Sodium borohydride solution	Beyotime Biotechnology Co. LTD	CAS No.:16940-66-2
Silver nitrate	Beyotime Biotechnology Co. LTD	CAS:7761-88-8
3,3', 5,5'- tetramethylbenzidine	Alibaba Group	CAS: 54827-17-7
Cell count Kit-8 kit	Beyotime Biotechnology Co. LTD	C0038
Critical commercial assays		
Electron spin resonance (ESR)	Beijing Zhongke Baitest Information Technology Co. LTD	BC231030-305
Transmission Electron Microscope	Beijing Zhongke Baitest Information Technology Co. LTD	BC230613-151
Experimental models: Cell lines		
CT26.WT (Mouse Colorectal Carcinoma Cells)	the Chinese Academy of Sciences Shanghai Cell Bank (Shanghai)	YML026
Experimental models: Organisms/strains		
BALB/c mice	Shanghai Slac Experimental Animal Co. LTD	021-57639280

EXPERIMENTAL MODE AND STUDY PARTICIPANT DETAILS

Materials

We purchased the ethanol from China National Pharmaceutical Chemical Reagent Co., Ltd., and the zinc acetate dihydrate from Shanghai Aladdin Technology Co., Ltd., Ltd., A solution of sodium borohydride and silver nitrate was provided by Shanghai Biyuntian Biotechnology Co., Ltd., and 3,3', 5,5'- tetramethylbenzidine (TMB) was purchased from Alibaba Group. cell count Kit-8 kit (cck-8 kit) was purchased from Shanghai Biyuntian Biotechnology Co., Ltd., Calcein/PI cell activity and cytotoxicity testing kit was purchased from Shanghai Biyuntian Biotechnology Co., Ltd., 2 ', 7' - Diacetate of dichlorofluorescein (DCFH-DA) was purchased from Shanghai Biyuntian Biotechnology Co., Ltd. Tian Biotechnology Co., Ltd., I obtained 5,5-dimethyl-1-pyrroline-N-oxide (DMPO) from Shanghai APExBIO, and JC-1 reagent kit from Yisheng Biotechnology Co., Ltd.

Cell line

We used CT-26 cells from the Chinese Academy of Sciences Shanghai Cell Bank (Shanghai) to study. Cells were incubated at 37°C and 5% CO_2 in DMEM complete medium containing 10% fetal bovine serum.

Animals

Six-week-old male BALB/c mice were obtained from Shanghai Slac Experimental Animal Co., Ltd. (Shanghai, China) and raised at Shanghai Tenth People's Hospital (Shanghai, China). The animal research has been approved by the Animal Ethics Committee of Shanghai Tenth People's Hospital. Mice were raised in a temperature-controlled environment (20-24°C) with a relative humidity of 50-60% and exposed to specific pathogens for 12 hours.

METHOD DETAILS

Synthesis of nanoparticles

Synthesis of ZnO nanorods

In a three-neck flask fitted with a condenser and a dropping funnel, dissolve 511 mg of zinc acetate dihydrate ($Zn(OAc)_2 \cdot 2H_2O$) in 35 mL of ethanol. Gradually add 35 mL of ethanol with 466 mg of sodium hydroxide (NaOH), stirring continuously to maintain room temperature and ensure uniform reactant mixing. Continue stirring for 30 minutes to complete the reaction. Transfer the mixture

to a 140 mL Teflon-lined autoclave, seal it, and heat to 160°C for 24 hours to facilitate the reaction. After the reaction, cool the autoclave to room temperature and collect the ZnO nanorods by centrifugation. Wash the ZnO nanorods thrice with ultrapure water and then with ethanol to remove impurities. Dry at 50°C to obtain the final sample.

Synthesis of ZnO@Ag nanoparticles

Suspend the prepared ZnO nanorods in ultrapure water to ensure uniform distribution. Slowly add a silver nitrate ($AgNO_3$) solution, stirring vigorously for 20 minutes to facilitate Ag deposition on the ZnO surface. Then, carefully add a pre-prepared ice-cold solution of sodium borohydride ($NaBH_4$) to moderate the reaction kinetics. Collect the ZnO@Ag nanorods by centrifugation post-reaction. This process forms a heterostructure, enhancing the sonodynamic and antimicrobial properties due to improved charge separation and increased reactive surface area.

Characterization of nanoparticles

Transmission Electron Microscopy (TEM) and elemental mapping

We used Transmission Electron Microscopy (TEM) and Energy Dispersive X-ray (EDX) spectroscopy for elemental mapping. Samples of ZnO@Ag NRs were prepared by dropping a small amount of the nanorod suspension onto a carbon-coated copper grid and allowing it to dry at room temperature. TEM images were captured using a JEOL JEM-2100 transmission electron microscope operated at an accelerating voltage of 200 kV. Images were acquired to observe the morphology and size distribution of the ZnO@Ag NRs. Elemental mapping was conducted using EDX spectroscopy attached to the TEM. The distribution of zinc (Zn), oxygen (O), and silver (Ag) was mapped by collecting EDX spectra at each pixel in the scanned area.

Electron spin resonance (ESR) spectroscopy for singlet oxygen detection

ESR spectroscopy was employed to detect singlet oxygen generation using 2,2,6,6-tetramethylpiperidine (TEMP) as a specific probe. TEMP reacts with $^1O_2$ to form a stable nitroxide radical (TEMP-$^1O_2$), which produces a characteristic 1:1:1 triplet ESR signal. This method is a reliable and established technique for detecting singlet oxygen in sonodynamic therapy systems.

In vitro biosafety evaluation and antitumor efficacy

CCK-8 assay protocol for testing the biocompatibility of nanoparticles

Inoculate CT26 cells into a 96 well culture plate, with 4000 cells per well, and incubate for 24 hours. Next, add different concentrations of ZnO separately ZnO@Ag (0, 3.125, 6.25, 12.5, 25, 50, 100) μ Incubate with a concentration of g/mL. After 24 hours, remove the culture medium and carefully wash three times with PBS for 5 minutes each time. Subsequently, replace the culture medium with DMEM containing 10% cell counting Kit-8 and continue to incubate for 1 hour. Detect the relative viability of cells by comparing the absorbance values of fluorescence spectrometers at 450 nm.

CCK-8 method for determining the cytotoxicity of nanoparticles

Inoculate CT26 cells into a 96 well culture plate, with 4000 cells per well. After incubation for 24 hours, add different concentrations of ZnO and ZnO@Ag (0, 3.125, 6.25, 12.5, 25, 50, 100) μg/mL. After 12 hours, irradiate with ultrasound for 1 minute. After 24 hours, remove the culture medium and wash it carefully three times with PBS, each time for 5 minutes. Replace the culture medium with DMEM containing 10% cell counting Kit-8 and continue to incubate for 1 hour. Using an enzyme-linked immunosorbent assay (ELISA) reader, measure the absorbance at 450 nm.

Calcein/PI staining experiment

Inoculate 10^5 CT26 cells per well in a 12 well plate, culture for 24 hours, and then add different combinations of materials to the culture medium for uniform dispersion. After 12 hours, irradiate with ultrasound for 1 minute. After co incubation for 24 hours, wash three times with PBS. After treatment, cells were stained using Calcein-AM (to stain live cells green) and Propidium Iodide (PI, to stain dead cells red) for 15 minutes, then washed three times with PBS carefully to remove excess impurities. Fluorescence images were captured using an inverted fluorescence microscope (Olympus IX73).

ROS generation detection

Inoculate CT26 cells into a 12 well plate with an initial density of 10^5 cells per well. Add materials ZnO into different pores ZnO@Ag. After incubation for 12 hours, use ultrasound Illuminate for 1 minute with a duty cycle of 50%. Cells treated with complete culture medium will be used as the control group. Treated CT-26 cells were incubated with DCFH-DA, and fluorescence images were taken using fluorescence microscope.

Flow cytometry analysis of apoptosis

Apoptosis was assessed using Annexin V-FITC/PI staining followed by flow cytometry. The preparation and treatment of cells were the same as descripted in 12.3.5. Treated cells were stained with Annexin V-FITC and PI according to the manufacturer's protocol and analyzed using a BD FACSCanto II flow cytometer. Data were processed using FlowJo software to determine the percentage of apoptotic cells.

Mitochondrial membrane potential

Mitochondrial membrane potential was assessed using JC-1 dye, which emits red fluorescence in healthy mitochondria and green fluorescence in depolarized mitochondria. The preparation and treatment of cells were the same as descripted in 12.3.5. Stained cells were imaged using a fluorescence microscope (Olympus IX73) with filters for JC-1 red and green emissions.

In vivo antitumor efficacy

Animal models establishment and intervention strategies

The treatment of mice was shown in Figure 7A. 30 six-week-old BALB/c mice were divided into 6 groups randomly. 100 μL of the CT26 cell suspension (containing 1×10^6 cells) was subcutaneously injected into the right flank of each mouse. 5 days after the injection, the tumors reach an approximate volume of 100 mm^3. Administer treatments was applied via tail vein injection at the specified dosage (3.5 mg/kg for ZnO or ZnO@Ag) at day0 and day 2. Then we apply ultrasound (US) treatment (1.5 W/cm^2, 50% duty cycle, 1 MHz) to the tumor area for 4 minutes on day 1 and day 3. To assess the *in vivo* antitumor efficacy, tumor volumes were measured using a digital caliper and calculated using the formula: Volume = (Length × $Width^2$) / 2 every other day. At day 14, the mice were killed and the tumors and major organs including lung, liver, spleen, kidney, and heart were harvested for further study.

Histological analysis

Tumor tissues and major organs were fixed in 10% formalin, and embedded in paraffin. Sections were stained with Hematoxylin and Eosin (H&E) for general histology and with TUNEL and Ki-67 to assess apoptosis and proliferation, respectively. Stained sections were imaged using a light microscope (Leica DM5000 B) equipped with a digital camera.

QUANTIFICATION AND STATISTICAL ANALYSIS

All data are shown as mean + SD unless otherwise noted. One-way ANOVA was used to analyze the data. Statistically significant differences were defined as p values less than 0.05. All significant differences were represented by symbols. '*' means p value < 0.05, '**' means p value < 0.01, '***' means p value < 0.001, '****' means p value < 0.0001.

ADDITIONAL RESOURCES

This study has not generated or contributed to a new website/forum or is not part of any clinical trial.